Evaluation of Mechanical and Corrosion Properties of Friction Stir-Welded AA6005-T6

Rodrigo José Contieri[a] ![ORCID], Ricardo Floriano[a], Mario Henrique Fernandes Batalha[b], André Ferrara Carunchio[b], José Eduardo May[c] ![ORCID], Alessandra Cremasco[a*] ![ORCID]

[a]*Universidade Estadual de Campinas, Faculdade de Ciências Aplicadas, Limeira, SP, Brasil.*
[b]*Instituto de Pesquisas Tecnológicas, Laboratório de Estruturas Leves, São José dos Campos, SP, Brasil.*
[c]*Instituto Nacional de Pesquisas Espaciais, São José dos Campos, SP, Brasil.*

The vast majority of advanced industrialized products are formed from the joining of individual components. However, when the joining must be permanent, welding is one of the most used processes. Among the welding processes, the Friction Stir Welding (FSW) process stands out in this category specially for producing joints with extremely high mechanical resistance and low distortions leading to modern automotive and aerospace applications. This study aimed to evaluate the mechanical and corrosion properties of FSW welded profiles of Aluminum AA6005 alloy as a function of the welding parameters. For this purpose, tensile and microhardness tests were performed, followed by a detailed microstructural analysis. The results showed that the high rotational speed provided tunnel-type defects which impair the mechanical properties, leading to a loss of efficiency. The corrosion properties results showed that the different welding conditions do not significantly affect corrosion characteristics but the changes observed are related to the dispersion of the precipitates in the Al matrix.

Keywords: *Friction Stir Welding, Aluminum alloy, X-ray microtomography, Corrosion resistance.*

1. Introduction

Aluminum and its alloys have important applications in the automotive and aerospace industry[1-3]. The mechanical strength of some aluminum alloys is in certain cases superior to low carbon steels. In addition, its excellent corrosion resistance and specific gravity of 2.7 g/cm³ (equivalent to 1/3 of the specific weight of steel) allow these alloys to be an alternative in the replacement of components or structural parts, aiming the reduction of weight and consequent payload increase.

However, even with the great interest of such industries for aluminum-based products, poor performance in some mechanical properties limits their use on large scale. If the performance of these alloys in service is similar to other alloys such as titanium alloys and steels, the diversity of industrial products based on Al alloys would be greater[4,5]. Thus, the challenges currently proposed require that new materials and processing routes must be developed that enable the improvement of the mechanical properties and consequently of applications, supplying the demands of the global market. Traditionally, the most used welding processes have as main source the electric arc welding and oxy-acetylene flame[6]. However, concerning the joining of aluminum alloys, the processes of electric arc welding that lead the material to fusion, are not the most recommended, because it generates in aluminum and its alloys, significant defects in welded joints, for example, cracks, distortions, porosities and residual stresses[7].

An alternative to the conventional joining process of aluminum and its alloys is obtained through the solid-state welding process known as Friction Stir Welding (FSW). In this process, a non-consumable high rotation tool consisting of a shoulder and a pin comes in contact with the parts to be joined and the heat generated by friction at the interface between the parts, promotes the coalescing of the materials resulting in the solid-state mixing between the parts, thus forming a weld joint. The parts to be joined are held under forging pressure during tool passing[8]. The FSW process has been much studied and its applicability has proved to be an alternative for several markets, such as automotive, aeronautics, aerospace, and naval, where the substitution of ferrous alloys for light aluminum alloys is of great interest. In this context, FSW has made great progress in joining aluminum alloys and the understanding of the microstructure evolution as a function of mechanical properties is very important for friction stir welded aluminum alloys.

Alinaghian et al.[9] reported that FSW can be used as an efficient solution to obtain high strength joints in nonferrous materials such as 2XXX, 6XXX and 7XXX series aluminum alloys, which due to the low weldability and high porosity, are classified as non-weldable by conventional welding processes. The advantages of this process come from the fact that it occurs in the solid-state, at a temperature below the melting point of the base material (maximum 80%), thus avoiding metallurgical problems arising from the phenomena acting in the solidification process. In addition, many of the drawbacks, usually observable in conventional welding processes, are avoided, such as soot emission, electric arc and spray presence, and noise pollution[10].

From the metallurgical point of view, different microstructures are generated by the FSW process. The extent of the different

*e-mail: acremasc@unicamp.br

microstructures formed is directly related to the process variables such as tool geometry and size, rotational speed and welding speed, and microstructural characteristics of the alloy to be joined[11]. According to Devaiah et al.[12] the welding process by FSW can be designed in a cause and effect diagram of Ishikawa type since the variables involved are numerous. In this way, more precise control and understanding of the variables involved leads to good quality welds with excellent physical, mechanical, and microstructural integrity. In this respect, few studies in the literature provide the systematic relationship of these processing variables and their influence on the different types of microstructures obtained.

The high strength AA6XXX (Al-Mg-Si) alloy is used mainly in a transportation industry among others[13] and several studies related to this class aluminum alloy (AA6082-T6; AA6061-T6; AA6056-T4 and T78) processed by FSW have been done in order to elucidate the microstructural development, as grain morphology and secondary particle, and the mechanical properties of joints, which are dependents of the thermo-mechanical cycle during the welding, aiming to establish the better window processing and improve the efficiency of process[14-16]. The low strength of welds obtained by FSW or by derivate process from FSW in 6XXX series alloy compared to base material (BM) occurs due welding defects on advancing side (AS) and/or retreating side (RS), as also can be associated to softening in the heat-affected zone (HAZ), which are governed by rotational speeds and welding speed[13,17].

However, studies related to FSW processing of AA6005-T6 are limited and focused on effects of parameters as welding speed[18], axial force[19], and comparison from different technologies derivate of conventional FSW according the tools profile[20] on joint quality, microstructural evolution and mechanical properties, but there is no published study regarding rotational speeds in the range evaluated in this work combined at welding speed and axial force suitable for industrial scale. A few variations on chemical composition, tempers condition or thickness plate can alter the microstructure development and consequently the joint properties, requiring new optimization of process parameters, as reported by Gallais et al.[16] for AA6056 alloy in T4 and T78 condition, which different nucleation sites on HAZ are verified in function of initial condition, with heterogeneous precipitation to T4 weld and a coarsening and partial dissolution precipitation to T78 weld.

Thereby, the different microstructures combinate to alloying elements segregation or mixture promoted from friction stir welding process can modify the alloy corrosion resistance. Studies have demonstrated FSW of aluminum alloys shows better corrosion resistance compared to a conventional welding processing[21,22], but tends to be inferior or even similar to the BM, showing intergranular attack and susceptibility to pitting corrosion due to the reducing grain size and increases of intermetallic particles according to process parameters[23,24]. Rambabu et al.[25] analyzed the effect

of tool pin profile, rotational speed, welding speed, and axial force on corrosion resistance of aluminum alloy AA2219 and concluded that hexagon tool profile combined to lower axial force, lower rotational speed and lower welding speed resulted in more noble corrosion pit potential.

The main problem in the joining of aluminum alloys obtained by the FSW process is generally encountered in the region of the welds, especially in the mixing zone or stir zone (SZ) and in the thermo-mechanically affected zone (TMAZ)[26]. In these areas, the intense plastic deformation and exposure to direct heat affect the microstructure of the material, changing its properties. Although the FSW process stands out for good quality welds in aluminum alloys (compared to conventional processes with an electric arc), some defects can still be observed[27]. The occurrence of these defects acts in an undesirable way in the point of view of the mechanical properties of the joints obtained by FSW. These defects have a direct relationship with the process variables, ranging from tool geometry and rotation and magnitude of the axial load to the forward speed. Therefore, the proper choice of processing variables allowed welds free of defects. In this context, the present research aims to investigate the influence of the FSW process parameters on the formation of defects in 6005-T6 Al alloy and its effects on mechanical and corrosion properties. By controlling the FSW process parameters, we expect to improve the efficiency of the FSW weld joints when compared to the BM.

2. Experimental Procedure

The experiments were carried out with AA6005-T6 aluminum alloy supplied by the Companhia Brasileira de Alumínio (CBA). Its chemical composition is presented in Table 1. The used welding station was an MTI (GG7 model). All FSW processing was performed with a constant welding speed of 300 mm/min and rotational speeds ranging from 1,000 rpm, 1,500 rpm and 2,000 rpm. The processing parameters were chosen after preliminary tests based on the optimization of the welding productivity on an industrial scale, ie, high welding speed. Welds were made using extruded plates with the following dimensions: 240×100×3 mm. The welding tool was made of structural steel (AISI H13) with a diameter of the shoulder of 20 mm, while the pin was 6 mm in diameter with 2.8 mm in length. Also, for all welds, the tool angle was 1° and shoulder penetration in the plate was set at 0.1 mm and the measurement control was performed by the machine position sensor. In addition, from the data acquisition system of the welding machine, the position and force parameters as a function of time were registered.

The microstructure analyses of the cross-sectional specimens were performed by the conventional metallographic procedure according to the ASTM-E3 standard and final electrochemical polishing[28]. The images were obtained using optical microscopy (Olympus, model BX60M) and scanning electron microscopy (SEM) by a Zeiss, model EVO
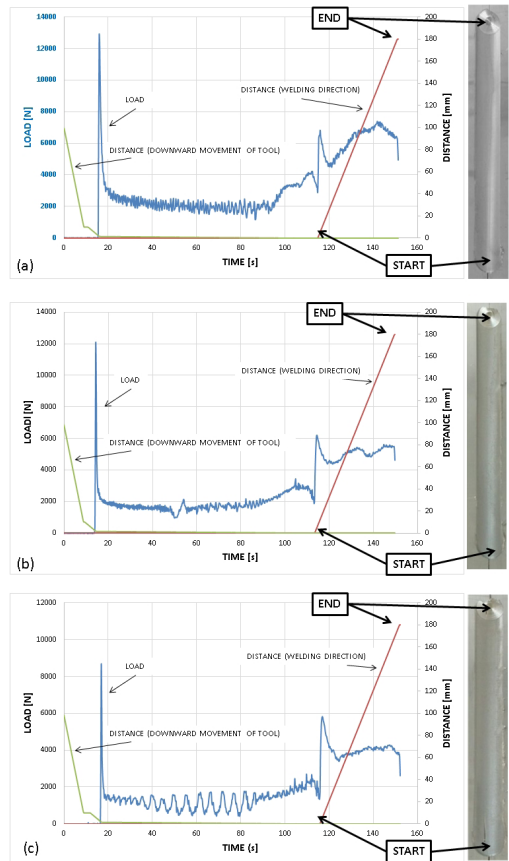
Table 1. Chemical composition (CC) for AA6005-T6 Aluminum alloy (wt%).

Elements	Al	Cr	Cu	Fe	Mg	Mn	Si	Ti	Zn
CC (wt%)	97.5-99	< 0.1	< 0.1	< 0.35	0.4-0.6	< 0.1	0.6-0.9	< 0.1	< 0.1

15. The detailed analysis of microstructure and intermetallic particles was obtained by high-resolution transmission electron microscopy (HR-TEM) using a Jeol, model JEM 3010 URP equipment, coupled with energy-dispersive X-ray spectroscopy and operating at 300 kV. The HR-TEM specimens were prepared from 3 mm diameter discs by grinding, polishing and Ar$^+$ ion milling. The tensile tests on welded specimens were performed on the transverse, i.e., perpendicular to the welding direction. The tests were conducted in a universal testing machine (EMIC, model DL2000) under a rate of 2 mm/min for determining the tensile strength (UTS), yield strength (YS) and elongation to failure (%El)[29]. The hardness profile of each specimen was measured using a Vickers hardness test (Buehler, model 2100) using loads of 300 gf applied for 15 s[30]. For a better investigation of the defects generated in the processing, X-ray microtomography analyzes were performed using a Bruker (model Skyscan 1272) with a source of 100 keV and 350 nm resolution equipment. The corrosion tests were carried out in a potentiostat (Autolab, model 302N) in aerated 3.5% NaCl solution. The specimen of BM and the welded zones (WZ) was surface polished using silicon carbide paper up to grade #1200, in order to obtain the same roughness for all the samples. The specimen area was 0.17 cm^2, including the welding and mixing zone. A saturated calomel electrode (SCE) was used as the reference electrode and a platinum rod as the counter electrode for the electrochemical measurements. An open-circuit potential (OCP) for every specimen was performed for 60 min. In the sequence, linear sweep voltammetry (LSV) was performed at 200 mV below to the open circuit potential of the material until a suitable voltage with a scan rate of 1 mV/s. The corrosion rate was obtained using the Tafel method. The pitting and corrosion potentials were also obtained. Additionally, the samples after the corrosion tests were analyzed by scanning electron microscopy (Tescan, model VEGA3).

Figure 1. Graphical representations of load and distance as a function of welding time at different rotational speeds of (a) 1,000 rpm, (b) 1,500 rpm and (c) 2,000 rpm at a constant welding speed of 300 mm/min. A macrography of the welding region showing the start and endpoints of welding in the plate is also included.

3. Results and Discussion

Figure 1 shows the processing curves obtained during the FSW welding as well as the macrography of the welding joint for each of the conditions tested. For all processing conditions, an abrupt increase in load is observed, at time around 15 s. It is a consequence of the moment when the tool comes into contact with the plate (downward movement of tool). Once the thermal and mechanical balance conditions have been established, the load stabilizes throughout processing. It is noteworthy that the process control was performed by position, i.e, the equipment changed the load as a function of the position in Z (shoulder penetration in the plate was set at 0.1 mm). A closer inspection of Figure 1a showed that the condition of lower tool rotation (1,000 rpm) required an average load of the machine between 5000 N and 7500 N during the joining process. Differently, when the rotation increases, Figure 1b-c, there is a clear decrease in the applied load, being for the maximum rotation (2,000 rpm), the load used was almost constant, around 4000 N. This result may be explained due to the variation of tool rotation which is associated to the welding speed and tool geometry that generates different thermal contributions in the material during the welding which probably affects the demanded friction. In this way, as a consequence of the plastic deformation employed, the heat

applied provides different annealing conditions (recrystallization), altering the resistance of the material to the tool. According to the thermal input equation modeled by Nelson and Wei[8], the energy generated during the process ranged from 0.72 kJ/mm to 1.05 kJ/mm from the lowest to the highest rotation. Also, in association with the studies of Sutton et al.[31] and Cederqvist and Reynolds[32], we could argue that, under the parameters used in this study, the thermal energies were found to be normal for the highest rotation, being inexpressive for the lower rotations. Bilgin et al.[33] obtained a similar relation during the increase of the welding speed in Al alloys joined by FSW process. They observed a gradual reduction of the thermal contribution with the increase of the welding speed and the torque, which was explained by the increase of both variables simultaneously, being the increase of the speed more accentuated. However, regardless of the load or thermal input conditions, the surface appearance of the welded joint showed no apparent differences as observed on macrographs from Figure 1 (right side). One reason for this can be related to the constant welding speed.

Figure 2a, b shows the representative stress-strain curves together with the mechanical properties results taking from the tensile testing of the Al joints welded at different rotational speeds. Each curve is the average value measured after three
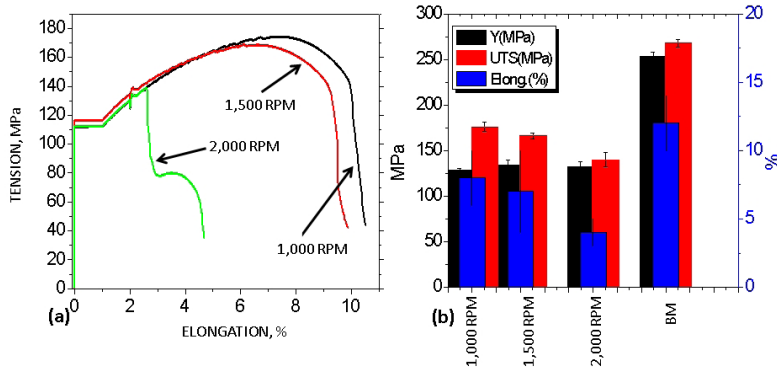
Figure 2. (a) Representative curve of tensile tests and (b) relation of mechanical properties of the extruded samples after FSW processing, where YS represents the yield strength, UTS the ultimate tensile strength, and ELONG the elongation.

tensile tests. According to the curves, it is possible to notice the constant behavior of the elastic modulus (65 GPa) and an evident loss of strength after the FSW process. As can be shown in Figure 2b, the ultimate tensile strength, yield strength and elongation of welded joints at different rotation speeds are lower than the BM. The values obtained for the ultimate tensile strength, yield strength and elongation of the BM are 188 MPa, 114 MPA and 15%, respectively. Even among the welded joints samples, there are slight variations in their values. In the same way, the ductility results showed a slow decrease after the FSW processing.

The values found for the ultimate tensile strength and yield strength are in good agreement with the expected values of welded specimens since a decrease in properties for welded components is predictable. Therefore, with those values, it is possible to evaluate which configuration of parameters generates the best efficiency of the joint when compared to the BM. In this way, it is clear that the condition of smaller rotation provides the best-welded joint. The efficiency attested for this condition was almost 70% compared to the BM, which refers to about 15% greater than the highest rotation applied. When we associate such results with the welding machine response, it is possible to observe a clear evidence between the thermal conditions imposed during the FSW process. The most interesting aspect of this behavior is about the representative curve obtained for 2,000 rpm in Figure 2a. After several test specimens, all curves showed a stress-strain pattern which is composed by two stages of deformation. In the first stage, the maximum stress applied to the material is around 130 MPa for deformation of 2.5% and in a second stage, it decreases to 80 MPa for deformation of 4%, indicating that the high speed of rotation also is influencing the flow of material and consequently the microstructural and mechanical aspects of the aluminum alloy.

Figure 3 provides the results obtained from the microhardness test of samples processed by FSW at different rotational speeds. In this figure, it is noticed that the general behavior of the hardness curve versus the distance is practically the same and the curve shows a "W" format. The average hardness of the BM was 78 HV and the hardness at the center of the joint or in the stir zone (SZ) was close to 62 HV for 1,000 and 1,500 rpm, while for the highest rotation of 2,000 rpm, the hardness was slightly lower, being around
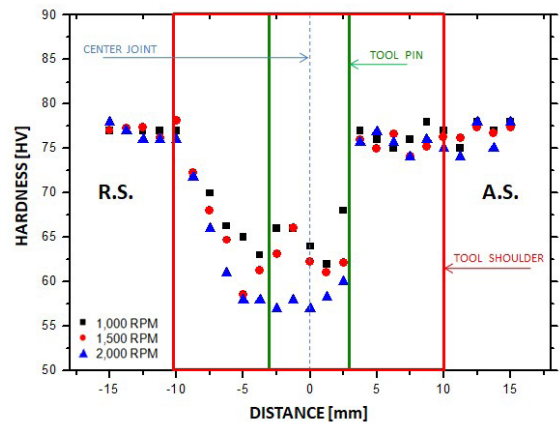
Figure 3. Profile of cross-section hardness of extruded samples after FSW processing. A.S.: advancing side; R.S.: retreating side.

58 HV. These results were expected mainly because in the stir- and mixing zone (SZ and MZ), the recrystallization of the material tends to eliminate the dislocations, differently from the region of the BM where the material still conserves the density of dislocations and grain size. Meanwhile, the heat affected (HAZ) and thermo-mechanically affected (TMAZ) regions are different from the BM. In the HAZ occurs a gradual elimination of dislocations and a slight increase in grain size due to the heat generated during the process. According to the hardness profile, possibly in the TMAZ, the temperature generated during processing enabled complete recrystallization, similar to the SZ. It is important to emphasize that second phase solubility effects must also be considered as an influence of the hardness profile. This gradual behavior can be well observed in the hardness profile between the positions of -10 mm and -5 mm from the tool retreating side (R.S). However, when observing the advancing side (A.S) of the tool, it is noted that the hardness transition was abrupt for the two largest rotations, which mechanically characterizes as a well-defined interface between the region of the BM and MZ.

By comparing the hardness profile with the geometry of the tool in terms of dimensions, it can be verified that the

interface between the two regions coincides exactly with the location of the tool pin in the A.S. Probably, this abrupt change of hardness is directly related to the flow of material during processing. According to simulations performed in a novel flow model for dissimilar material by Kadian and Biswas[34], the flow of material is affected by the geometry of the pin, as well as by the heat generated during the process. This impacts the hardness of material, since it modifies the formation of the MZ during the welding process directly affecting the amount of plastically mixed materials. It can thus be suggested that in a condition of greater thermal input and consequently lower resistance of the material, the flow of metal around the tool pin is facilitated, which is a non-gradual way, that competes with another region in the most unfavorable thermal condition. Unlike the retreating side (R.S), the A.S tends to interact less with the side material, since the front of the tool concentrates more interaction.

Figure 4 shows the macrostructure profile of FSW AA6005-T6 joints with 1,000, 1,500 and 2,000 rpm. By looking into the type of joint formed, the complete union between the two parts of the sheet is observed, once the processing has reached the root of the joint. For all conditions evaluated, one can see the clear difference between the SZ and the BM. Also, it is possible to observe some differences between the A.S and R.S regions. On the retreating side, as observed in the hardness profile, the microstructural transition occurs gradually since the existing material under the R.S. shoulder included extruded metal only, unlike the advancing side which has an obvious transition interface. As a result of the flow lines, A.S. shoulder included extruded and rotated metal. Such behavior was also observed in the study performed by Zhu et al.[35]. When the material is located in the front of the tool pin and it moves to the R.S., the speed of the material flow is reduced due to an insufficient driving force and consequently hampering the movement on the A.S.

Additionally, the color gradient as shown in Figure 4, produced by the chemical etching during the metallographic preparation of the welded joint cross-section, revealed that the plastic deformation process is followed by complete recrystallization since the color contrast is related to the crystallographic orientation of grains and in this case, the grains have almost a similar orientation.

Closer inspection in the macrostructure (Figure 4) showed around the interface in the A.S. that there are some defects, like voids. This defect seems to be more pronounced when the rotational speeds increases. The Figure 5a presents images with higher magnification carried out by SEM for AA6005-T6 samples welded by FSW at rotational speed of 2,000 rpm, it is possible to notice that the defect is formed between two distinct flow regions – between the HAZ and SZ. According to Zhu et al.[35], the flow of material during the FSW process plays a major role, since it defines the formation of defects in the joint. Probably, this defect could be initiate in the SZ or in the TMAZ. The void caused by the material flow at A.S. shoulder could be originated at the triple junction of pin surface, SZ and TMAZ as detailed at Figure 5a. The formation of the crack from the vertices of the defect, which allows us to affirm as being one of the main causes of the mechanical behavior presented in the tensile tests, as the deformation in two stages shown in Figure 2a. The request of the material in the first stage occurs until the beginning of the nucleation of the crack from the void. With the start of the crack, a second deformation mode is configured, which denotes the second stage evidenced at Figure 2.

Figure 5b shows the fractography obtained after tensile testing of the sample welded at 2,000 rpm of rotational speed. The fractographs revealed regions of ductile fracture characteristics, represented by the formation of micromechanisms of deformation such as dimples and regions of fragile fracture with a smoother appearance, which corroborates with defects observed and mechanical strength and ductility values. Elangovan and Balasubramanian[36] also reported the presence of defects with high thermal input at different aluminum alloys. In a similar direction, Kim et al.[37] reported volumetric defects with high welding speed, which resulted in "hot" welds and the reason reported by the authors is that an abnormal stirring of the material is caused by a temperature gradient between the near-surface material and the close to the root of the weld. In this way, the thermal input is a
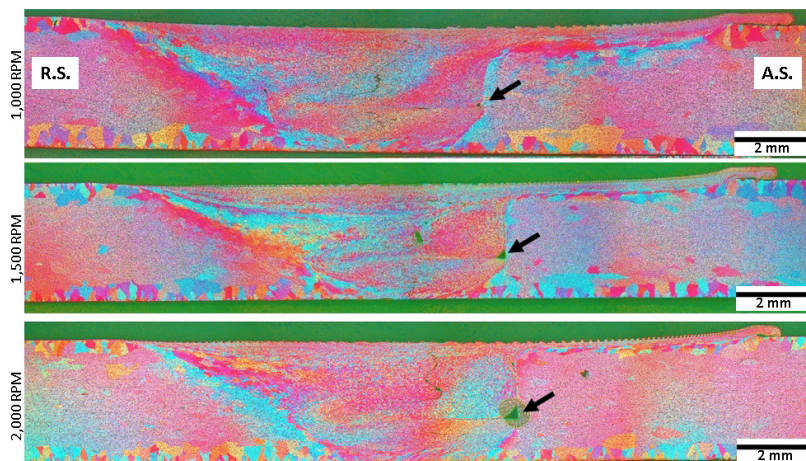

Figure 4. Optical macrograph results of the extruded samples AA6005-T6 after welding by FSW at different tool rotational speeds.

determining factor to ensure a quality weld, a combination of parameters that results in a defect-free weld is desired.

Regions of TMAZ and SZ were examined by OM and TEM analysis to reveal the presence of precipitates in the alloy after being processed by FSW and the images are shown in

Figure 6. According to Figure 6a-c, it is possible to observe that the regions composed by TMAZ and SZ presented second phase precipitation which are homogeneously dispersed over the aluminum matrix. Such precipitate distribution was expected since the $Al_{12}(Fe,Mn)_3Si$ phase is desirable for extruded aluminum
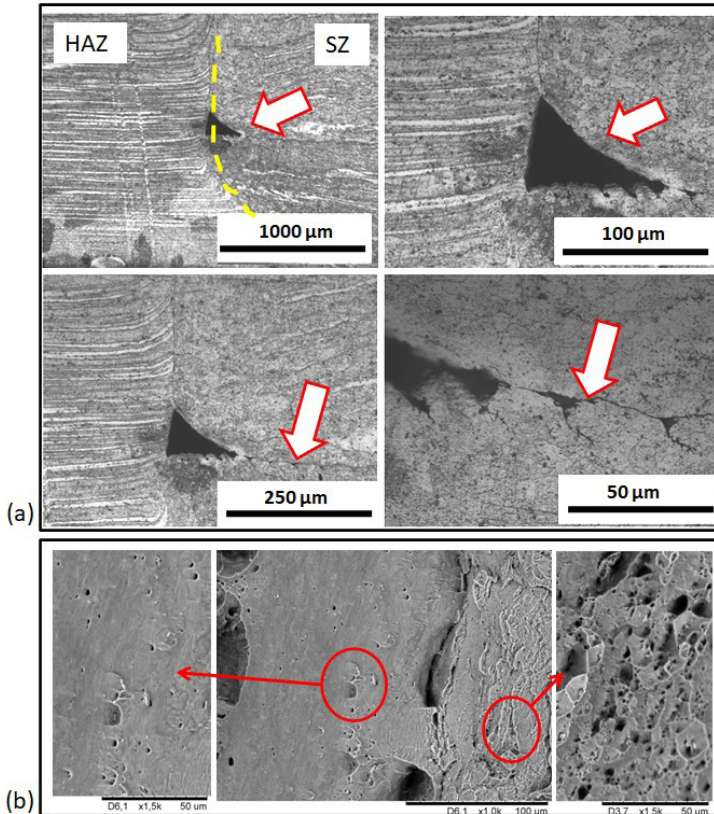
Figure 5. (a) Microstructural detail and defect formation and (b) fractography obtained after tensile testing of the sample with 2,000 rpm rotational speed.
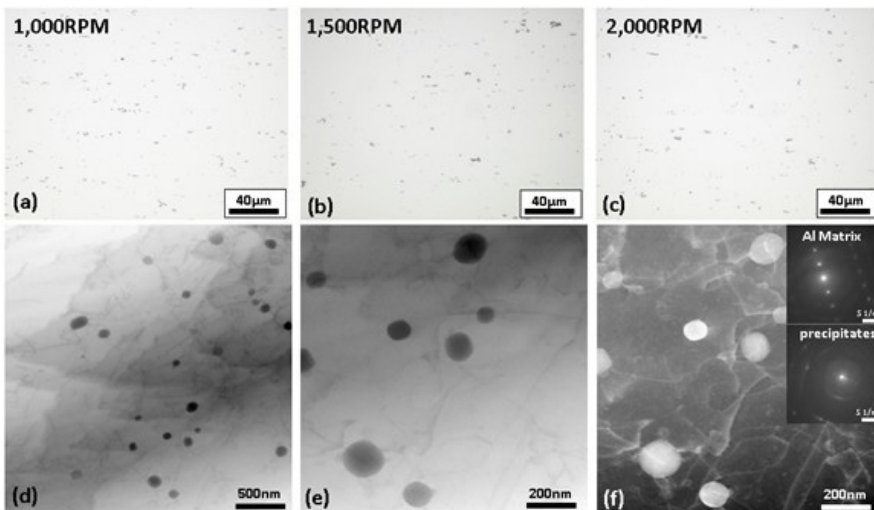
Figure 6. Optical and Electronic Transmission Microstructure highlighted for the formation of second-phase precipitates α - $Al_{12}(Fe,Mn)_3Si$: (a-c) TMAZ and SZ regions; Mg_2Si: (d-f) TEM and diffraction pattern (on the right) of the SZ region preceded with 1,500 rpm.
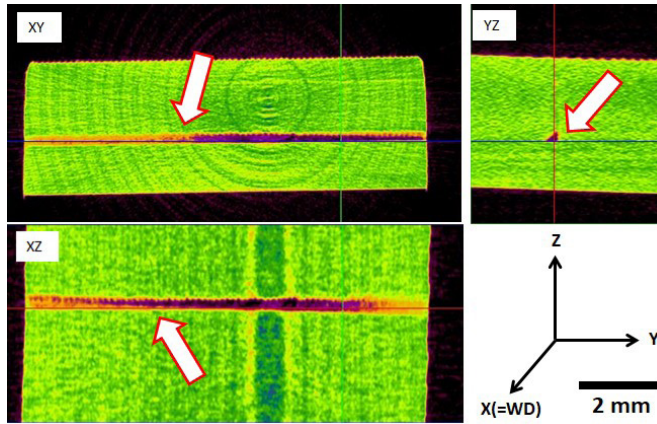
Figure 7. Images of X-ray microtomography of the sample processed with 2,000 rpm of rotation.

alloys, as it acts as a facilitator of the forming process, as well as enabling the reduction of grains size by the phenomenon of impingement. A detailed analysis of the volumetric fraction and sizes of these second-phase precipitates reveals a slight difference between the processing conditions. For the 1,000 rpm rotational speed, the number of precipitates was greater than 2.4% with an average size of $4.6 \pm 0.3 \, \mu m^2$, differing for the highest rotations of 1,500 rpm and 2,000 rpm, where the values were, respectively, 1.7% ($3.7 \pm 0.3 \, \mu m^2$) and 1.0% ($3.4 \pm 0.3 \, \mu m^2$).

From TEM images shown in Figure 6d-f, it was possible to observe in detail the distribution of precipitates on the AA6005-T6 aluminum matrix. The strengthen phase Mg_2Si (β phase) was not statistically clearly detected (since, due to the characteristics of the transmission analysis, the observation region is very small when compared to the bulk), certainly due to possible solubilization caused by the thermal processing conditions, since the hardness results for the region under analysis presented a significant reduction. Owing to the rise of temperature, the β phase started to dissolve into the matrix, leading to the reduction of its volume fraction. While for the α-$Al_{12}(Fe,Mn)_3Si$ phase, the variations of area fraction and particle size were hardly distinguished because of the high dissolution temperature for Si-rich particle (α phase). However, due to the low volume fraction observed for this phase, we cannot attribute its influence on the mechanical properties.

To evaluate the extent of the defect produced by the processing conditions of 2,000 rpm tool rotation, X-ray microtomography analyzes were performed throughout the entire weld joint as can be shown in Figure 7. From this figure, it is possible to confirm that the void is a tunnel-type defect. Thus, it should be emphasized that this type of analysis is important since investigations in only two dimensions could generate the idea that this kind of defect can be classified as void defect. By looking into the tomography images, in the direction of the longitudinal planes, XY and XZ, it is verified that the tunnel formed along the direction of the tool is almost constant in terms of size and morphology. This implies that only the conditions imposed by the processing parameters act on the defect formation. According to Liu and Wu[38], the formation of the tunnel-type defect occurs due to a delay in the flow of material. This delay generates the formation of three interconnected subzones that originates the defect. However, according to the study, the main cause
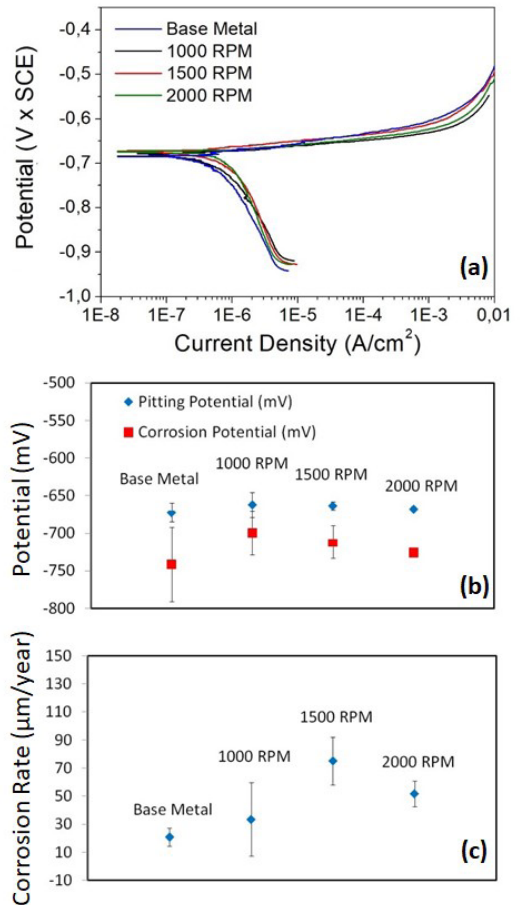

Figure 8. (a) Potentiodynamic polarization curves; (b) Corrosion and pitting potentials and (c) Corrosion rate obtained by Tafel extrapolation method for BM and welded joints at different rotational speeds.

of the defect is due to the insufficient flow of material from the R.S. toward the A.S. and the scarcity of material transfer to the underside of the tool is the second reason.
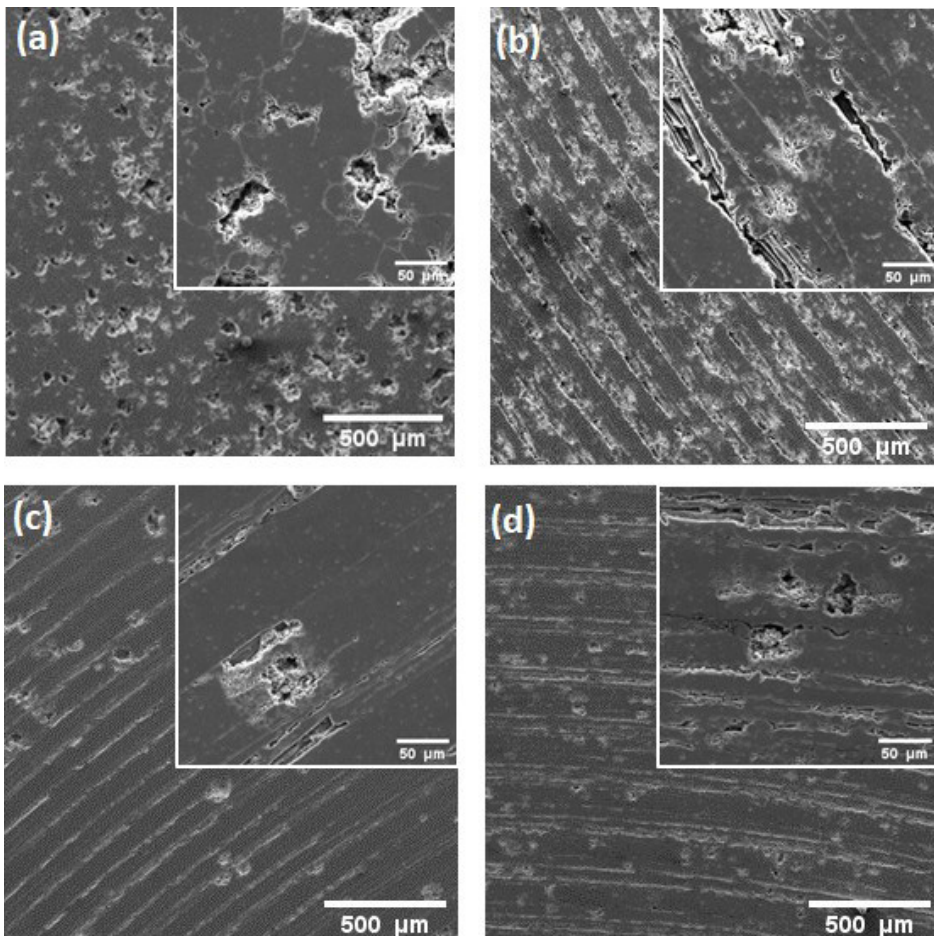
Figure 8a shows the potentiodynamic polarization curves for BM and FSW welded joints at different rotational speeds

conducted in a naturally aerated aqueous with 3.5% of NaCl solution. The results showed that the corrosion potential and pitting potential were not significantly changed after the processing of welding by FSW, as indicated in the graph shown in Figure 8 (b). Therefore, the corrosion rate obtained by Tafel method, Figure 8c, shows that all the samples have similar corrosion rates with an overlap standard deviation. Rambabu et al.[25] affirm that the corrosion rate is more sensitive to change in axial force than to the changes in rotational speed and welding speed, as also that the tool profiles affect the corrosion resistance of friction stir welded joints of AA2219 aluminum alloy. The corrosion rates obtained are in good agreement with the values obtained by Li et al.[39] for a similar 6005 aluminum alloy tested in 3.5% NaCl solution, about 33,5 µm/year. In a similar direction, Fahimpour et al.[21] analyzing the corrosion behavior of 6061 aluminum alloy welded by FSW observed comparable pitting potentials, around -0.65 V, for BM and WS, as also observed in this current paper.

The SEM images displayed in Figure 9 show that the localized pitting is preferentially formed at grain boundaries for BM (Figure 9a) and at the fusion solidification lines for WS (Figure 9b-d). Additionally, an increase in visual density of pitting is verified in the FSW samples welded at lower rotational speeds. As already known, aluminum alloys form a protective oxide layer in surface and inclusions, grain boundaries or intermetallic particles results in a non-homogeneous film that favors the cathodic reactions of oxygen reduction followed by anodic dissolution matrix and the pit initiation[16]. In the same way, the intermetallic particles composed by Al and Mg are anodic for Al matrix, while that the intermetallic precipitates comprising of Al, Fe and Mn, as observed by TEM images of FSW samples, are cathodic[32]. Those cathodic intermetallic particles form galvanic cell with an Al-matrix and act as a cathode to oxygen reduction. The apparently increases of pitting corrosion susceptibility at 1,000 rpm rotational speed are associated with high dispersion of the precipitates in the alloy matrix and near to grain boundary, which tends to dissolve in superior rotational speeds. When looking at the micrographs shown in Figure 6, the potential effect of second-phase precipitates on pitting formation is clear. Compounded by the processing condition, which due to the low speed, the less solubilized particles $Al_{12}(Fe,Mn)_3Si$ and therefore generates more interfaces with a high potential for corrosion.

Figure 9. SEM micrographs of the surface of the AA6005 after potentiodymic polarization test under 3.5% NaCl solution to (a) BM and for welded joints at rotational speeds of (b) 1,000 rpm (c) 1,500 rpm and (d) 2,000 rpm.

4. Conclusions

In this study, we evaluated the mechanical and corrosion properties of friction stir welded AA6005 aluminum alloy at different rotational speeds. The main findings of this study are summarized below.

(1) The mechanical properties results indicated that in terms of yield strength and ultimate tensile strength, all tested parameters presented good values for welded joints except for ductility that was low for higher rotations;

(2) The main cause of deterioration of mechanical properties is due to the formation of a tunnel-type defect, resulting from the heterogeneous material flow generated by speed differences between the A.S. and the R.S. in association with the low flow of material below to the tool pin;

(3) The high rotation of the tool increases the energy generated in the process that reduces the force required due to the increase in plasticity. However, the low forces employed modifies the material flow under the tool which in turn results in the formation of defects;

(4) The corrosion results indicated that the pitting potential and corrosion resistance were not significantly affected for the FSW welding parameters.

(5) SEM images after corrosion testing revealed that the visual pitting dispersion density is lower to high rotational speeds due to the partial dissolution of second phase precipitates as also confirmed by the TEM analysis.

5. Acknowledgments

6. References

1. Milagre MX, Mogili NV, Donatus U, Giorjão RAR, Terada M, Araujo JVS, et al. On the microstructure characterization of the AA2098-T351 alloy welded by FSW. Mater Charact. 2018;140:233-46. http://dx.doi.org/10.1016/j.matchar.2018.04.015.

2. Du C, Wang X, Pan Q, Xue K, Ni M, Liu J. Correlation between microstructure and mechanical properties of 6061-T6 double-side FSW joint. J Manuf Process. 2019;38:122-34. http://dx.doi.org/10.1016/j.jmapro.2019.01.010.

3. Adamowski J, Szkodo M. Friction Stir Welds (FSW) of aluminium alloy AW6082-T6. J Achiev Mater Manuf Eng. 2007;20:403-6.

4. Ungureanu CA, Das S, Jawahir IS. Life-cycle cost analysis: *aluminum versus steel* in passenger cars. TMS Annu Meet. 2007:11-24.

5. Zhou J, Wan X, Li Y. Advanced aluminium products and manufacturing technologies applied on vehicles presented at the EuroCarBody Conference. Mater Today-Proc. 2015;2(10 Pt A):5015-22. http://dx.doi.org/10.1016/j.matpr.2015.10.091.

6. He ZB, Peng YY, Yin ZM, Lei XF. Comparison of FSW and TIG welded joints in Al-Mg-Mn-Sc-Zr alloy plates. Trans Nonferrous Met Soc China. 2011;21(8):1685-91. http://dx.doi.org/10.1016/S1003-6326(11)60915-1.

7. Sattari S, Bisadi H, Sajed M. Mechanical properties and temperature distributions of thin friction stir welded sheets of AA5083. Int J Mech Appl. 2012;2(1):1-6. http://dx.doi.org/10.5923/j.mechanics.20120201.01.

8. Nelson TW, Wei L. Correlation of microstructures and process variables in FSW HSLA-65 steel. Weld J. 2011;90:95-101.

9. Alinaghian I, Honarpisheh M, Amini S. The influence of bending mode ultrasonic-assisted friction stir welding of Al-6061-T6 alloy on residual stress, welding force and macrostructure. Int J Adv Manuf Technol. 2018;95(5-8):2757-66. http://dx.doi.org/10.1007/s00170-017-1431-6.

10. Tova R, Gambaro C, Volpone M. Friction stir welding: an innovative seam technology. Weld Int. 2003;17(1):36-42. http://dx.doi.org/10.1533/wint.2003.3053.

11. Jayaraman M, Sivasubramanian R, Balasubramanian V. Effect of process parameters on tensile strength of friction stir welded cast LM6 aluminium alloy joints. J. Mater. Sci. Technol. 2009;25:655-664. http://dx.doi.org/10.1016/s1003-6326(13)62506-6.

12. Devaiah D, Kishore K, Laxminarayana P. Optimal FSW process parameters for dissimilar aluminium alloys (AA5083 and AA6061) using taguchi technique. Mater Today Proc. 2018;5(2):4607-14. http://dx.doi.org/10.1016/j.matpr.2017.12.031.

13. Jacquin D, Guillemot G. A review of microstructural changes occurring during FSW in aluminium alloys and their modelling. J Mater Process Technol. 2021;288:116706. http://dx.doi.org/10.1016/j.jmatprotec.2020.116706.

14. Wan L, Huang Y, Lv Z, Lv S, Feng J. Effect of self-support friction stir welding on microstructure and microhardness of 6082-T6 aluminum alloy joint. Mater Des. 2014;55:197-203. http://dx.doi.org/10.1016/j.matdes.2013.09.073.

15. Trueba L Jr, Torres MA, Johannes LB, Rybicki D. Process optimization in the self-reacting friction stir welding of aluminum 6061-T6. Int J Mater Form. 2018;11(4):559-70. http://dx.doi.org/10.1007/s12289-017-1365-4.

16. Gallais C, Denquin A, Bréchet Y, Lapasset G. Precipitation microstructures in an AA6056 aluminium alloy after friction stir welding: characterisation and modelling. Mater Sci Eng A. 2008;496(1-2):77-89. http://dx.doi.org/10.1016/j.msea.2008.06.033.

17. Costa MI, Leitão C, Rodrigues DM. Influence of post-welding heat-treatment on the monotonic and fatigue strength of 6082-T6 friction stir lap welds. J Mater Process Technol. 2017;250:289-96. http://dx.doi.org/10.1016/j.jmatprotec.2017.07.030.

18. Simar A, Bréchet Y, de Meester B, Denquin A, Pardoen T. Microstructure, local and global mechanical properties of friction stir welds in aluminium alloy 6005A-T6. Mater Sci Eng A. 2008;486(1-2):85-95. http://dx.doi.org/10.1016/j.msea.2007.08.041.

19. Liu X, Liu H, Wang T, Wang X, Yang S. Correlation between microstructures and mechanical properties of high-speed friction stir welded aluminum hollow extrusions subjected to axial forces. J Mater Sci Technol. 2018;34(1):102-11. http://dx.doi.org/10.1016/j.jmst.2017.11.015.

20. Esmaily M, Mortazavi N, Osikowicz W, Hindsefelt H, Svensson JE, Halvarsson M, et al. Bobbin and conventional friction stir welding of thick extruded AA6005-T6 profiles. Mater Des. 2016;108:114-25. http://dx.doi.org/10.1016/j.matdes.2016.06.089.

21. Fahimpour V, Sadrnezhaad SK, Karimzadeh F. Corrosion behavior of aluminum 6061 alloy joined by friction stir welding and gas tungsten arc welding methods. Mater Des. 2012;39:329-33. http://dx.doi.org/10.1016/j.matdes.2012.02.043.

22. Maggiolino S, Schmid C. Corrosion resistance in FSW and in MIG welding techniques of AA6XXX. J Mater Process Technol. 2008;197(1-3):237-40. http://dx.doi.org/10.1016/j.jmatprotec.2007.06.034.

23. Gharavi F, Matori KA, Yunus R, Othman NK, Fadaeifard F. Corrosion behavior of Al6061 alloy weldment produced by friction stir welding process. J Mater Res Technol. 2015;4(3):314-22. http://dx.doi.org/10.1016/j.jmrt.2015.01.007.

24. Esmaily M, Mortazavi N, Osikowicz W, Hindsefelt H, Svensson JE, Halvarsson M, et al. Corrosion behaviour of friction stir-welded AA6005-T6 using a bobbin tool. Corros Sci. 2016;111:98-109. http://dx.doi.org/10.1016/j.corsci.2016.04.046.

25. Rambabu G, Balaji Naik D, Venkata Rao CH, Srinivasa Rao K, Madhusudan Reddy G. Optimization of friction stir welding parameters for improved corrosion resistance of AA2219 aluminum alloy joints. Def Technol. 2015;11(4):330-7. http://dx.doi.org/10.1016/j.dt.2015.05.003.

26. Cui L, Yang X, Zhou G, Xu X, Shen Z. Characteristics of defects and tensile behaviors on friction stir welded AA6061-T4 T-joints. Mater Sci Eng A. 2012;543:58-68. http://dx.doi.org/10.1016/j.msea.2012.02.045.

27. Dehghani M, Amadeh A, Akbari Mousavi SAA. Investigations on the effects of friction stir welding parameters on intermetallic and defect formation in joining aluminum alloy to mild steel. Mater Des. 2013;49:433-41. http://dx.doi.org/10.1016/j.matdes.2013.01.013.

28. ASTM: American Society for Testing and Materials. ASTM E3-11: Standard Practice for Preparation of Metallographic Specimens. West Conshohocken: ASTM; 2017.

29. ASTM: American Society for Testing and Materials. ASTM E8M-16: Standard Test Methods for Tension Testing of Metallic Materials. West Conshohocken: ASTM; 2012.

30. ASTM: American Society for Testing and Materials. ASTM E92-17: Standard Test Methods for Vickers Hardness and Knoop Hardness of Metallic Materials. West Conshohocken: ASTM; 2009.

31. Sutton MA, Reynolds AP, Yang B, Taylor R. Mixed mode I/II fracture of 2024-T3 friction stir welds. Eng Fract Mech. 2003;70(15):2215-34. http://dx.doi.org/10.1016/S0013-7944(02)00236-9.

32. Cederqvist L, Reynolds AP. Factors affecting the properties of friction stir welded aluminum lap joints. Weld J. 2002;80:281-7.

33. Bilgin MB, Meran C. The effect of tool rotational and traverse speed on friction stir weldability of AISI 430 ferritic stainless steels. Mater Des. 2012;33:376-83. http://dx.doi.org/10.1016/j.matdes.2011.04.013.

34. Kadian AK, Biswas P. The study of material flow behaviour in dissimilar material FSW of AA6061 and Cu-B370 alloys plates. J Manuf Process. 2018;34(Pt A):96-105. http://dx.doi.org/10.1016/j.jmapro.2018.05.035.

35. Zhu Y, Chen G, Chen Q, Zhang G, Shi Q. Simulation of material plastic flow driven by non-uniform friction force during friction stir welding and related defect prediction. Mater Des. 2016;108:400-10. http://dx.doi.org/10.1016/j.matdes.2016.06.119.

36. Elangovan K, Balasubramanian V. Influences of tool pin profile and welding speed on the formation of friction stir processing zone in AA2219 aluminium alloy. J Mater Process Technol. 2008;200(1-3):163-75. http://dx.doi.org/10.1016/j.jmatprotec.2007.09.019.

37. Kim YG, Fujii H, Tsumura T, Komazaki T, Nakata K. Three defect types in friction stir welding of aluminum die casting alloy. Mater Sci Eng A. 2006;415(1-2):250-4. http://dx.doi.org/10.1016/j.msea.2005.09.072.

38. Liu XC, Wu CS. Elimination of tunnel defect in ultrasonic vibration enhanced friction stir welding. Mater Des. 2016;90:350-8. http://dx.doi.org/10.1016/j.matdes.2015.10.131.

39. Li W, Chen X, Chen B. Effect of aging on the corrosion behavior of 6005 Al alloys in 3.5 wt% NaCl aqueous solution. J Mater Res. 2018;33(12):1830-8. http://dx.doi.org/10.1557/jmr.2018.86.